Nanoscale

PAPER

View Article Online
View Journal | View Issue

Cite this: *Nanoscale*, 2023, **15**, 19629

Transparent metal oxide interlayer enabling durable and fast-switching zinc anode-based electrochromic devices†

Bing Xu,[a] Jingwei Chen, *[a] Ping Li,[a] Yujia Ouyang,[a] Yu Ma,[a] Huanlei Wang*[a] and Haizeng Li *[b,c]

Growing energy and environmental challenges have imposed higher requirements for the development of novel multifunctional energy storage and energy-saving devices. Electrochromic devices having similar configurations and working mechanisms with secondary batteries exhibit promising applications in dual-functional electrochromic-energy storage (ECES) devices. Electrochromic Prussian blue (PB) as typical battery cathodes are of great interest for ECES devices although they suffer from poor stability and limited capacity. In this study, a transparent metal oxide (NiO nanosheets) interlayer was incorporated to enhance the structural stability and capacity of PB while offering enlarged optical modulation (ΔT) and accelerated switching kinetics in the NiO/PB film. Impressively, the NiO/PB nanocomposite film exhibited a high areal capacity of 50 mA h m^{-2} and excellent electrochemical stability, simultaneously manifesting a large ΔT (73.2% at 632.8 nm), fast switching time (t_c = 1.4 s, t_b = 2.6 s) and higher coloration efficiency (CE = 54.9 cm^2 C^{-1}), surpassing those of the bare PB film (ΔT = 69.1% at 632.8 nm, t_c = 1.6 s, t_b = 4.1 s, CE = 50.9 cm^2 C^{-1}). Finally, a prototype zinc anode-based electrochromic device assembled with NiO/PB nanocomposite film exhibited a self-bleaching function and ΔT retention of up to 92% after 1000 cycles, and a 100 cm^2 large area device was also demonstrated for high performance. Such a transparent metal oxide interlayer has enabled the construction of durable and fast-switching dual-functional zinc anode-based electrochromic devices and will inspire more efforts in designing novel multifunctional ECES devices.

Received 28th September 2023,
Accepted 17th November 2023

DOI: 10.1039/d3nr04902g

rsc.li/nanoscale

Introduction

In recent years, with the rapid development of electronic technology and transformation of fossil energy, energy shortage and environmental deterioration have become increasingly serious, designing novel energy storage and energy-saving platforms has become a strategic direction for energy development.[1–6] Electrochromic smart windows have attracted wide attention due to the efficient modulation of visible and near-infra-red (NIR) light transmittance and thus savings in heat, ventilation, and air-conditioning (HVAC) energy consumption.[7–9] Electrochromism refers to the optical property (transmittance, absorbance, reflectance) variation in electrochromic materials (ECMs) or electrochromic devices (ECDs) upon the application of electric pulses (current or potential).[10,11] The reversible optical and electrochemical behavior, low energy consumption and charge storage capability have enabled the application of ECDs in the fields of smart windows, displays, optically adjustable electronic components, and others.[2,12–15] In general, ECDs are composed of a transparent substrate, transparent conductor, electrochromic layer, electrolyte, and ion storage layer.[16] Owing to the similarity to secondary batteries in configuration and working mechanism, ECDs are also endowed with energy storage capability and exhibit broad application prospects.[17] Noteworthily, ECDs with high coloration efficiency (CE) and fast switching normally require low charge density and large response in optical density, while energy storage devices need high charge density to provide sufficient capacity.[18] As such, the conflict between high CE and high capacity in ECES devices is to be resolved through the fabrication of advanced ECMs. Conventional intercalation-based ECDs usually face problems, such as the strong corrosion of H^+, high cost of Li^+, and large radius of Na^+ and

[a]*School of Materials Science and Engineering, Ocean University of China, Qingdao 266100, China. E-mail: chenjingwei@ouc.edu.cn, huanleiwang@ouc.edu.cn*
[b]*Institute of Frontier & Interdisciplinary Science, Shandong University, Qingdao 266237, China. E-mail: haizeng@sdu.edu.cn*
[c]*Shenzhen Research Institute of Shandong University, Shenzhen, Guangdong, 518057, China*

† Electronic supplementary information (ESI) available. See DOI: https://doi.org/10.1039/d3nr04902g

K^+, which have inspired researchers to explore multivalent ion intercalation-based ECDs.[19–21] Multivalent zinc-ions are considered attractive charge carriers for realizing next-generation electrochromic devices with high capacity and fast response due to the low cost, low redox potential (−0.76 V *vs.* SHE standard hydrogen electrode), high theoretical specific capacity (820 mA h g^{-1}), and safety in aqueous electrolytes of the Zn anode, and the high charge density of Zn^{2+}.[22,23]

Transition metal compounds are extensively studied as ECMs due to fast switching and excellent cycling stability, such as WO_3,[24] TiO_2,[25] V_2O_5,[26] MoO_3,[27] NiO,[28] and Prussian blue (PB).[29] Interestingly, PB has a high voltage plateau for excellent energy density and is widely employed as cathodes of secondary batteries.[30,31] PB has a cubic crystal structure with the formula of AFe(III)[Fe(CN)$_6$], where A is generally an alkali metal or ammonia.[32] The cyanide group acts as a bridge connecting two transition metal ions, Fe(III) and Fe(II) are alternately arranged at the corners of the cubic lattice to form the unique three-dimensional (3D) cubic structure.[33] The open 3D diffusion channels of PB can facilitate ion transport, thus realizing fast switching and large optical modulation (ΔT).[34] However, poor adhesion with conductive substrates, structural collapse due to repeated ion insertion/deinsertion during cycling and unsatisfactory capacity further limit the applications of PB-based ECES devices.

Introducing a nano-sized support template between active ECMs and the substrate has been proven to be an effective method to improve the performance of ECDs.[35–37] Chen *et al.* obtained an array of TiO_2@PB core–shell nanostructures with high specific surface by introducing TiO_2 nanorods between fluorine doped tin oxide (FTO) and PB.[38] One-dimensional TiO_2 nanorods provide unidirectional electron transport channels and expand the active surface area of ECMs.[38,39] However, the TiO_2@PB nanoarray only exhibits a mediocre ΔT (48%), slow switching time (t_b = 2.2 s, t_c = 6.2 s), without demonstrating energy storage capability. $Ni(OH)_2$ and NiO are extensively studied in various fields including catalysis,[40] supercapacitors,[41] and EC[42,43] for their open framework structure, high porosity, large surface area, excellent stability, and environmentally friendly properties.[44] The electrochemical active nickel hydroxide (β/γ-NiOOH) on the surface of NiO can be reduced to nickel hydroxide (α/β-$Ni(OH)_2$).[45] In particular, NiO as an ECM itself can be switched between a highly transparent state and gray-black neutral color in an alkaline solution depending on the reversible redox reaction between Ni^{2+} and Ni^{3+}, and is also a typical electrode material for energy storage, making it a potential candidate for constructing electrochromic batteries.[18,46]

In this work, a transparent metal oxide interlayer was synthesized *via* optimized chemical-bath deposition and annealing, after which NiO/PB nanocomposite films were obtained by further electrodeposition. $Ni(OH)_2$/PB was also synthesized for comparison. Notably, NiO/PB nanocomposite films demonstrated a high areal capacity of 50 mA h m^{-2} at a current density of 0.05 mA cm^{-2} and excellent electrochemical stability. In addition, the NiO/PB nanocomposite electrode exhibited a large ΔT (73.2% at 632.8 nm), fast switching (t_c = 1.4 s, t_b = 2.6 s), and high CE (54.9 cm^2 C^{-1}), ΔT retention of 92% (1000 cycles), outperforming those of bare PB and $Ni(OH)_2$/PB. Eventually, NiO/PB nanocomposite films were coupled with a zinc anode to obtain a 100 cm^2 bifunctional ECES, demonstrating the advances of such a nanocomposite film in constructing dual-functional ECES devices.

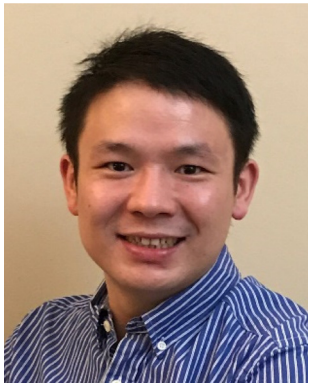

Haizeng Li

Haizeng Li obtained his Ph.D. in 2016 from the State Key Laboratory for Modification of Chemical Fibers and Polymer Materials, China. He then started his postdoctoral research with Prof. Abdulhakem Y. Elezzabi at the University of Alberta, Canada. After that, he joined Shandong University as a professor at the Institute of Frontier and Interdisciplinary Science and the School of Energy and Power Engineering. His current research interests include electrochromic devices, wearable electronics, energy storage, and radiative heat transfer.

Experimental section

Synthesis of $Ni(OH)_2$ nanosheets and NiO nanosheets

All reagents were of analytical grade and used without further purification. Nickel chloride hexahydrate was purchased from Macklin, ammonium chloride, and sodium hydroxide were purchased from Sinopharm Chemical Reagent Co. Fluorine doped tin oxide (FTO) coated glass was produced by Wuhan Jingge Solar Technology Co. FTO was used as a substrate and cleaned in acetone, anhydrous ethanol and deionized (DI) water by ultrasonication for 15 min, and then dried at 60 °C. $Ni(OH)_2$ nanosheets were synthesized by a modified chemical-bath deposition method.[44] The precursor solution contained $NiCl_2$ (37.5 mM), NH_4Cl (200 mM), and NaOH (68.75 mM), and was dissolved by magnetic stirring for 5 min. 20 mL of the above solution was transferred to a 50 mL container, FTO (2 cm × 2 cm) was dipped into the solution with the conductive side facing down, and heated at 55 °C for 6 hours. After that, FTO coated with $Ni(OH)_2$ nanosheets were washed with DI water and dried at 60 °C. Finally, the prepared $Ni(OH)_2$/FTO was annealed in air at 300 °C for 2 h and naturally cooled to room temperature to obtain NiO nanosheets/FTO.

Preparation of PB, $Ni(OH)_2$/PB and NiO/PB nanocomposite films

Potassium ferricyanide and ferric chloride hexahydrate were purchased from Macklin, and potassium chloride was purchased from Sinopharm Chemical Reagent Co. PB films were

synthesized on both bare FTO, $Ni(OH)_2$/FTO and NiO/FTO, respectively, using a typical electrodeposition step.[47] The deposition precursor solution was a mixed aqueous solution containing $K_3[Fe(CN)_6]$ (10 mM), $FeCl_3$ (10 mM), and KCl (50 mM). The CHI760E electrochemical workstation was employed for the three-electrode electrodeposition, with a platinum sheet as the counter electrode, Ag/AgCl as the reference electrode, and FTO, $Ni(OH)_2$/FTO and NiO/FTO as the working electrodes. A constant current density of -50 μA cm^{-2} was applied for 300 s. After that, the electrodes were washed several times with DI water and anhydrous ethanol. Finally, the electrodes were dried at 60 °C for 12 h.

Characterization

The microscopic morphology of the nanocomposite films was observed using scanning electron microscopy (Gemini SEM 300) and transmission electron microscopy (TEM, JEOL 2010F). The phase composition and surface chemistry of the samples were characterized by powder X-ray diffraction (XRD, Bruker D8) and X-ray photoelectron spectroscopy (XPS, Thermo Scientific K-Alpha). Specifically, powders for XRD and TEM analysis were scraped from the surface of the FTO-coated glass. Raman spectra were collected using a laser Raman spectrometer (HORIBA LabRAM HR800, laser excitation: 532 nm).

All electrochemical tests were performed on an electrochemical workstation (CHI760E, Shanghai Chenhua Instruments, Inc.) using a conventional three-electrode test system with a Pt sheet as the counter electrode, Ag/AgCl as the reference electrode, 1 M KCl as the electrolyte, and the prepared nanofilms as working electrodes. The optical properties of the nanocomposite films and switching kinetics were studied using a UV-Vis spectrophotometer (UV-2600i, SHIMADZU). The electrochemical and electrochromic performance of the zinc anode-based electrochromic device was tested using nanocomposite films as a cathode and zinc foil as an anode with 1 M KCl–0.1 M $ZnSO_4$ as a mixed electrolyte.

Results and discussion

Morphology and physical characterization

Since metal salts are typically water-sensitive, the rapid hydrolysis process at low temperatures produces amorphous products with polydispersity, and thus high temperatures (hydrothermal treatment or calcination) are required to achieve a high degree of crystallization.[48] However, hydrothermal and calcination synthesis are not favorable to fabricating EC electrodes in ECDs due to the difficulty in morphology control and the limited option of transparent conductive substrates. Deposition on different substrates under mild conditions (low temperature and atmospheric pressure) would greatly facilitate the fabrication of EC electrodes and thus wide application of ECDs.[44,49] In our work, $Ni(OH)_2$/FTO was first synthesized employing a modified chemical-bath deposition method at only 55 °C for 6 h.[44] The specific reaction process can be described as follows:[44]

$$NH_4^+ + OH^- \leftrightarrow NH_3 \cdot H_2O \quad (1)$$

$$Ni^{2+} + xNH_3 \leftrightarrow [Ni(NH_3)_x]^{2+} \quad (2)$$

$$Ni^{2+} + 2OH^- \leftrightarrow Ni(OH)_2 \quad (3)$$

The hydrogen bonding (N–H–O) between the nitrogen atom in NH_3 and the hydrogen atom of the surface hydroxyl group of $Ni(OH)_2$ causes selective adsorption of NH_3 on the (001) crystal planes of $Ni(OH)_2$, resulting in the formation of single-crystal $Ni(OH)_2$ nanosheets.[44,50] $Ni(OH)_2$/FTO electrodes are converted to NiO/FTO after annealing at 300 °C for 2 h in air. PB, $Ni(OH)_2$/PB, and NiO/PB electrodes were obtained by subsequent electrodeposition on bare FTO, $Ni(OH)_2$/FTO, and NiO/FTO substrates, respectively. The detailed synthesis procedure of NiO/PB is shown in Fig. 1.

Fig. S1a and b† shows the SEM images of bare PB and $Ni(OH)_2$ nanofilms. The $Ni(OH)_2$ nanofilms are composed of interconnected nanosheets (thickness 10–15 nm) with a length of ~500 nm. Previous studies have suggested that the nanosheets grown vertically on glass substrate did not detach even after sonication due to the strong bonding between Ni $(OH)_2$ nanosheets and substrate.[44,48,51] The SEM image of NiO in Fig. 2a shows that there is no significant change in the network structure of $Ni(OH)_2$ nanosheets after annealing. Fig. 2b and c presents the top-view and cross-sectional SEM observations of NiO/PB, displaying the well-preserved network structure of NiO nanosheets and the uniform coating of PB nanoparticles. The thicknesses of NiO nanosheets and PB films were about 250 nm and 280 nm, as seen in Fig. 2c, respectively. The uniform coating of PB on NiO can be further evidenced from the elemental mapping in Fig. 2f. Coordination water generated in the PB lattice during the synthesis in aqueous solutions often renders problems of lattice distortion, low coulombic efficiency, and structural instability,[52–57] thus prolonged heating of PB is required to reduce the amount of lattice water. As such, observable cracks can be seen in the PB films (Fig. 2b). Interestingly, this unique hierarchical structure allows effective electrolyte penetration into the abundant channels between NiO nanosheets and PB films, which effectively ensures PB exposure to the electrolyte, shortening the ion diffusion distance and simultaneously alle-

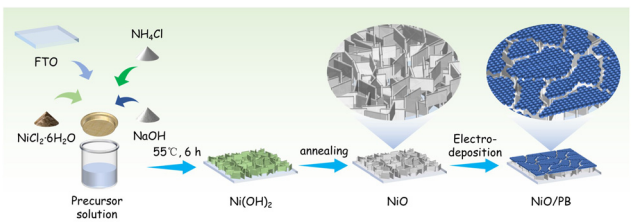

Fig. 1 Schematic illustration of the preparation process of NiO/PB.

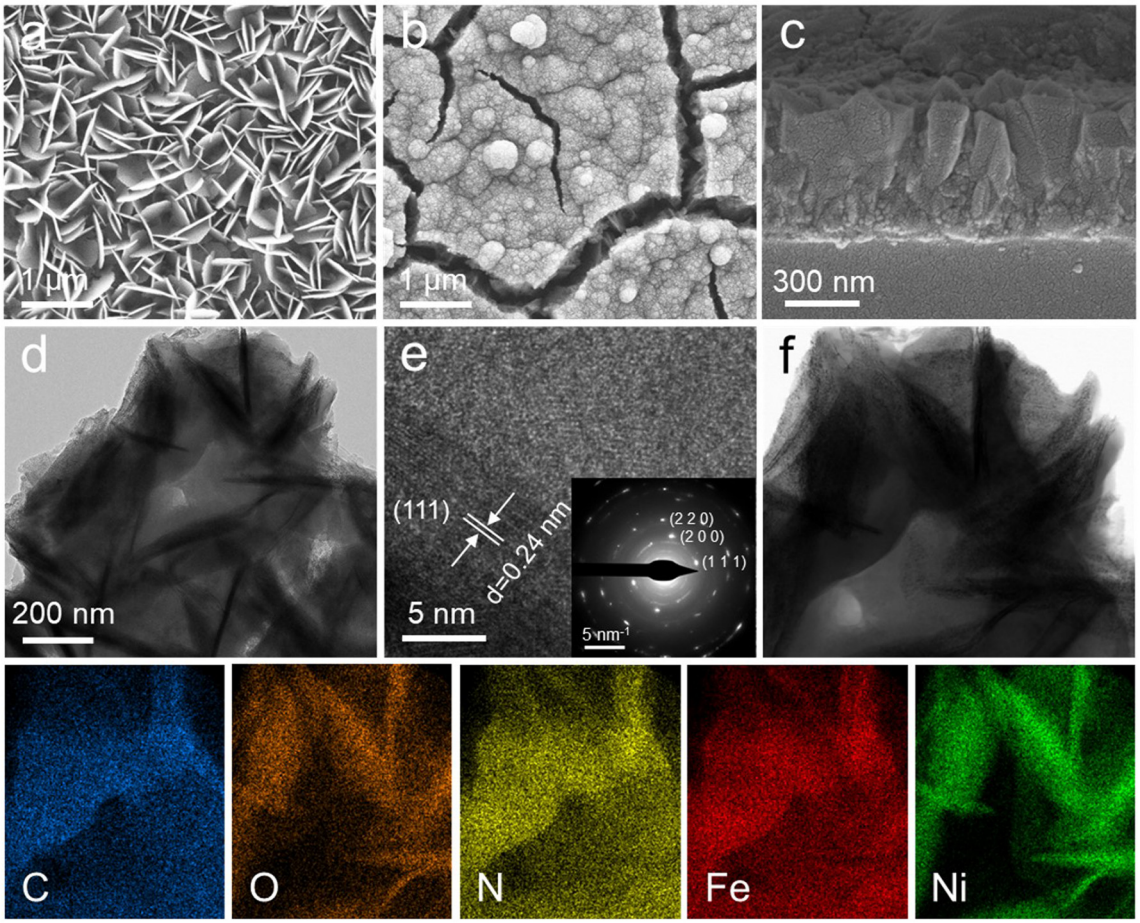

Fig. 2 Electron microscopic characterization of NiO/PB. SEM images of (a) NiO and (b) NiO/PB. (c) Cross-section SEM image of NiO/PB. (d) TEM image of NiO/PB. (e) High resolution image (HRTEM) of NiO/PB. (f) HADDF-STEM image and corresponding elemental mapping of NiO/PB.

viates the volume expansion of PB during cycling. In contrast, the compact bare PB films, electrodeposited directly on the FTO (Fig. S1a†), are less stable against repeated ion insertion/deinsertion. Additionally, the crystal structure of NiO/PB nanocomposite films was analyzed using the transmission electron microscope (TEM). As shown in Fig. 2d, the well-defined boundary in the nanocomposite films demonstrates the fine contact of NiO nanosheets with PB nanoparticles.[58,59] The high-resolution transmission electron microscopy (HRTEM) image (Fig. 2e) clearly illustrates the lattice structure of the NiO/PB nanocomposite films. The uniform lattice fringes with a lattice spacing of 0.24 nm match the (111) plane of NiO, and the corresponding selected area electron diffraction (SAED) pattern shows clear pattern matching (111), (200), and (220) crystal orientations of NiO, confirming the well-crystallization of the prepared NiO nanosheets.

X-ray diffraction (XRD) analysis was employed to determine the crystal structure of different nanocomposite films. The diffraction peaks centered at 19.3°, 33.1°, and 38.5° corresponded to the (001), (100), and (101) lattice planes of $Ni(OH)_2$ (JCPDF#14-0117, Fig. S2†), and the diffraction peaks centered at 37.2°, 43.3°, and 62.9° correspond to the (111), (200) and (220) lattice planes of NiO (JCPDF#47-1049, Fig. 3a), which indicates the complete transformation of $Ni(OH)_2$ into NiO after annealing. Raman spectra (Fig. 3b) revealed the characteristic bands of PB, including –Fe–CN–Fe– at 276 cm^{-1}, –Fe–C– at 537 cm^{-1}, and –C≡N– at 2157 cm^{-1}, confirming the successful deposition of PB on NiO.[60,61] Furthermore, XPS analysis was performed to explore the chemical composition of NiO/PB nanocomposite films. XPS survey spectra (Fig. 3c) of NiO/PB composite nanofilms confirmed the presence of C 1s, N 1s, O 1s, Fe 2p, and Ni 2p peaks. The high-resolution spectra of C 1s, N 1s, and Fe 2p were fitted with the peak separation employing the Gaussian–Lorentzian function, as shown in Fig. 3d–f. The C 1s spectrum has been deconvoluted into three peaks located at 284.8 eV, 286.5 eV, and 288.6 eV, which are attributed to C–C, C≡N, and C═O (Fig. 3d), respectively. The deconvoluted three peaks in the N 1s spectrum located at 397.8 eV, 399.7 eV, and 402.3 eV are ascribed to C≡N–Fe, C≡N, and N–O, respectively (Fig. 3e). As shown in Fig. 3f, the Fe 2p high-resolution spectrum could be fitted into four main peaks at 708.5 eV, 712.1 eV, 721.2 eV, and 722.2 eV, corresponding to Fe^{II} 2p 3/2, Fe^{III} 2p 3/2, Fe^{II} 2p 1/2, and Fe^{III} 2p 1/2 of PB, respectively.

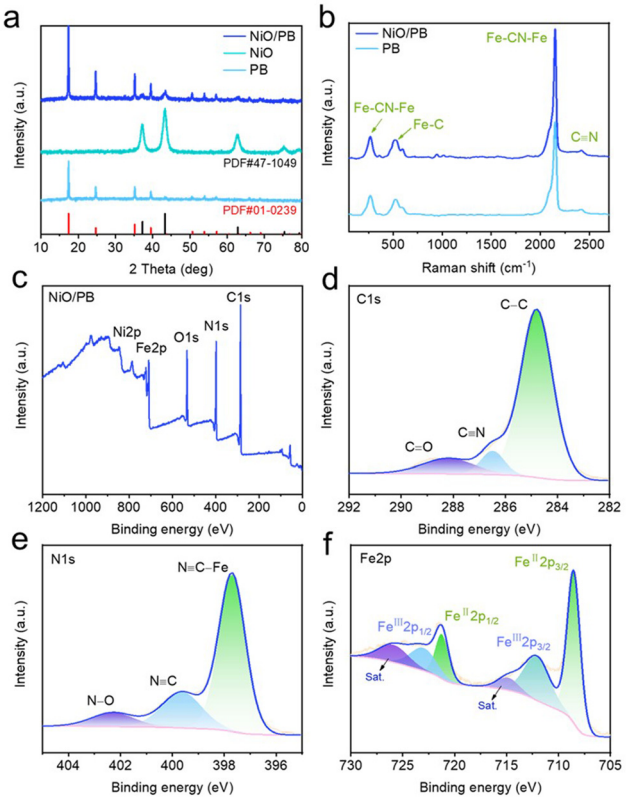

Fig. 3 Crystal and chemical structure characterization of PB, NiO, and NiO/PB. (a) XRD patterns of PB, NiO, and NiO/PB. (b) Raman spectra of PB and NiO/PB. (c) XPS survey spectra of NiO/PB. High resolution (d) C 1s, (e) N 1s and (f) Fe 2p XPS spectra of NiO/PB.

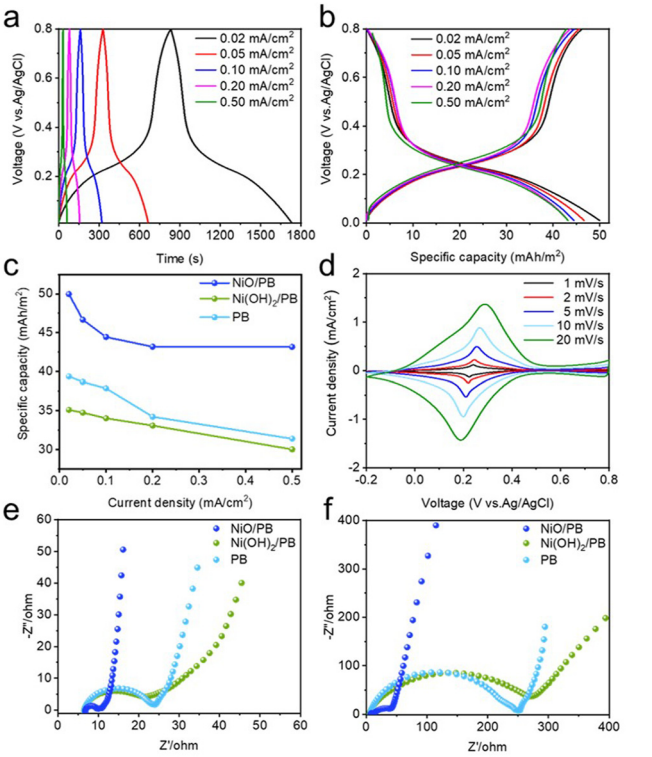

Fig. 4 Electrochemical performances of PB, $Ni(OH)_2$/PB, and NiO/PB. a, (b) GCD curves of NiO/PB at different current densities. (c) Specific areal capacities of PB, $Ni(OH)_2$/PB, and NiO/PB at different current densities. (d) CV curves of NiO/PB under various sweep rates. Nyquist plots of PB, $Ni(OH)_2$/PB, and NiO/PB (e) before and (f) after cycling.

Electrochemical performance evaluation

With the successful preparation of PB, $Ni(OH)_2$/PB, and NiO/PB, electrochemical tests were performed on these films in a three-electrode configuration to evaluate their electrochemical performances (Fig. 4 and S3†). Fig. 4a shows the galvanostatic charge/discharge (GCD) profiles of the NiO/PB nanocomposite films at different current densities. The charge/discharge plateau agrees with the redox peaks observed in cyclic voltammograms (CV) curves of Fig. 4d, corresponding to the redox reaction between Fe^{II} and Fe^{III}. The areal capacity of NiO/PB was quantified (Fig. 4b) based on the GCD curves and compared with that of PB and $Ni(OH)_2$/PB. Notably, the NiO/PB nanocomposite films exhibited an areal capacity of 50 mA h m^{-2} at 0.02 mA cm^{-2} and maintained 43.2 mA h m^{-2} when the current density was increased to 0.5 mA cm^{-2}, showing a superior rate capacity to that of PB and $Ni(OH)_2$/PB (Fig. 4c, Fig. S4a–d†). The cyclic voltammograms (CV) curves of NiO/PB under different scan rates were also collected as shown in Fig. 4d. The redox peak polarization increased linearly with enlarged sweep rates, indicating the excellent electrochemical reversibility of NiO/PB. In addition, NiO/PB showed higher peak currents (Fig. 4d) compared to PB (Fig. S3e†) and Ni $(OH)_2$/PB (Fig. S3f†) under the same scan rates. The small redox peak polarization, higher peak currents, and superior rate performance indicated favorable electrochemical reversibility and kinetics in NiO/PB. To evaluate the electrochemical stability of different electrodes, cycling stability tests were performed using CV at 20 mV s^{-1} (Fig. S4†). The CV curves of PB and $Ni(OH)_2$/PB showed slight degradation in the first 5 cycles and suffered from serious deterioration after 100 cycles. Impressively, the CV curves of NiO/PB were highly overlapped (Fig. S4e and f†), with the integrated area retention of 99.7% and 98.9% after 5 and 100 cycles, respectively, demonstrating significantly enhanced electrochemical stability of NiO/PB compared to PB and $Ni(OH)_2$/PB. In addition, the SEM images of NiO/PB (Fig. S5†) and PB (Fig. S6†) after 100 CV cycles similarly illustrated the promising cycling stability of NiO/PB. Electrochemical impedance spectroscopy (EIS) of PB, $Ni(OH)_2$/PB, and NiO/PB before and after CV cycling were also collected. The diameter of the semi-circle at the high-medium frequency region in Nyquist plots indicating the charge transfer resistance (R_{ct}). It was seen that the NiO/PB nanocomposite films presented a much lower and relatively stable charge transfer resistance (R_{ct}) before and after cycling (Fig. 4e and f), while the R_{ct} values of PB, $Ni(OH)_2$/PB were largely increased after cycling. The superior electrochemical performance of NiO/PB was evidenced from GCD, CV, cycling, and EIS measurements, which may be attributed to several reasons: (1) NiO nanosheets interlayer can effectively anchor the PB layer; (2) NiO nanosheets play an indispensable role in reducing the R_{ct} of PB, allowing easy charge transfer and improving material

utilization;[62,63] (3) the loose and porous structure of NiO/PB provides adequate contact with the electrolyte and higher electrochemical activity, simultaneously alleviating the volume expansion caused by ion insertion/deinsertion. The poor electrochemical performance of $Ni(OH)_2$/PB may be caused by poor electrical conductivity and high R_{ct} of $Ni(OH)_2$. Furthermore, to explore the capacity contribution of NiO in NiO/PB nanocomposite films, CV and GCD tests of NiO were performed (Fig. S7†), yet NiO showed pseudocapacitive behavior with the areal capacity of only ~3 mA h m^{-2}, indicating the minimal contribution of NiO to the areal capacity of NiO/PB.

Electrochromic performance characterization

In order to construct dual-functional zinc anode-based electrochromic devices, the electrochromic performances of PB, $Ni(OH)_2$/PB, and NiO/PB were evaluated by employing a two-electrode configuration with a zinc foil as the counter electrode and KCl–$ZnSO_4$ as the electrolyte. The UV-vis transmittance spectra of the colored (1.8 V for 20 s) and bleached NiO/PB (0.6 V for 20 s) were collected in the wavelength range of 400–800 nm, as shown in Fig. 5a. NiO/PB exhibited a large ΔT of 73.2% (@632.8 nm) when switched from transparent to blue, which is larger than PB (69.1%@632.8 nm, Fig. S8a†) and $Ni(OH)_2$/PB (52.1%@632.8 nm, Fig. S9a†). Coloration efficiency (CE) is one of the most important properties of electrochromism, which is defined as[64]

$$CE = \Delta OD/\Delta Q = \log(T_b/T_c)/\Delta Q \quad (4)$$

where ΔOD is the optical density, ΔQ is the injected charge, and T_b and T_c represent the transmittance in the bleached and colored states, respectively. By applying a linear fit to the optical density–charge density curve during NiO/PB coloration (Fig. 5b), the CE of NiO/PB was calculated as 54.9 cm^2 C^{-1}, higher than those of PB (50.9 cm^2 C^{-1}, Fig. S8b†) and $Ni(OH)_2$/PB (40.4 cm^2 C^{-1}, Fig. S9b†). A higher CE value indicates that the device can achieve large optical modulation with a small charge input.[61] Dynamic transmittance measurements were performed at 632.8 nm to evaluate the switching kinetics. As shown in Fig. 5c, the bleaching time (t_b) and coloration time (t_c) of NiO/PB were quantified to be 2.6 s and 1.4 s, respectively, notably faster than those of PB (t_b = 4.1 s, t_c = 1.6 s, Fig. S8c†) and $Ni(OH)_2$/PB (t_b = 13.9 s, t_c = 13.8 s, Fig. S9c†). Furthermore, the transmission spectra and *in situ* transmittance response of NiO (Fig. S10†) were employed to specify the effect of NiO on the optical properties of NiO/PB composite films. The results showed that NiO had negligible transmittance variation and did not contribute to the electrochromic performance in the NiO/PB film. The large ΔT probably originated from the stacking effect of NiO and PB, and the fast reaction kinetics may be attributed to the unique framework structure of NiO/PB that provided a large specific surface area and shortened the ion diffusion path. In contrast, the compact PB layer suffers from slow switching time. As for $Ni(OH)_2$/PB, the low electrical conductivity and high R_{ct} of $Ni(OH)_2$ resulted in lower ΔT and a longer switching time.

Investigation of zinc anode-based electrochromic devices

The excellent electrochemical and electrochromic performances of the NiO/PB electrode inspired us to construct a dual-functional zinc anode-based electrochromic device. The charging of the electrochromic device causes the coloration of NiO/PB and discharging renders bleaching, presenting dual functions for the ECES. The synchronous transmittance variation during the GCD process (current density of 0.10 mA cm^{-2}) is shown in Fig. 6a. During discharging, the Zn anode was oxi-

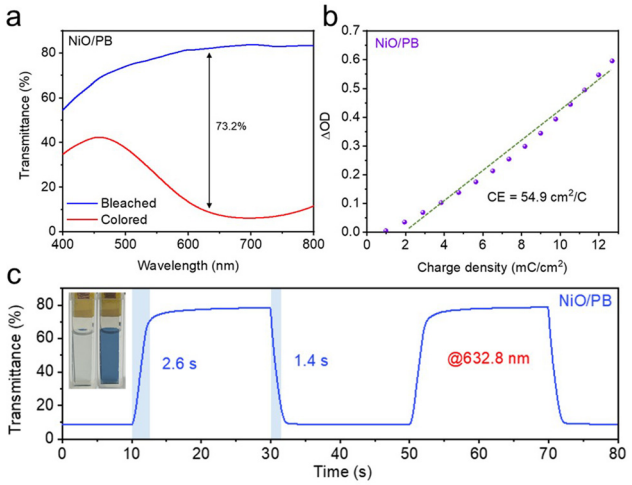

Fig. 5 Electrochromic performance of NiO/PB. (a) Transmittance spectra of NiO/PB in colored and bleached states at 400–800 nm. (b) *In situ* optical density *versus* charge density at 632.8 nm for NiO/PB during coloration. (c) *In situ* transmittance response of NiO/PB at 632.8 nm under potential steps (0.6 V and 1.8 V, each for 20 s) and digital photographs of NiO/PB in both colored and bleached states (inset).

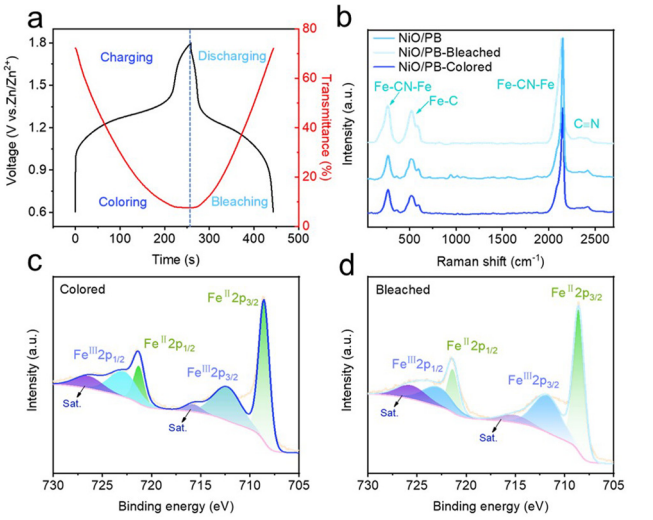

Fig. 6 (a) GCD curves at current densities of 0.1 mA cm^{-2} and simultaneous transmittance (@632.8 nm) evolution. (b) Raman spectra of NiO/PB in various states (original, colored, and bleached). High-resolution XPS spectra of Fe 2p in NiO/PB at (c) colored and (d) bleached states.

dized to release Zn^{2+} and PB in the cathode was reduced with K^+ insertion and bleached from the dark blue to the transparent state. Reversely, the charging of the electrochromic device causes Zn^{2+} reduction on the Zn anode and PB oxidation with K^+ extraction, along with coloration of the NiO/PB cathode, giving ΔT of more than 60% (@632.8 nm).

To further explore the electrochemical mechanism of the electrochromism in the zinc anode-based electrochromic devices, *ex situ* Raman spectra coupled with *ex situ* XPS were performed on NiO/PB in original, colored (Fig. S11†), and bleached (Fig. S12†) states. In Raman spectra, the characteristic peaks of PB were detected in different states of NiO/PB, without significant variation in the relative intensity or peak shift, indicating the excellent structural stability of NiO/PB during charging/discharging (coloration/bleaching) (Fig. 6b). The high-resolution XPS spectra of Fe 2p are demonstrated in Fig. 6c and d, showing the presence of Fe^{II} and Fe^{III} in the three states. The Fe^{II}/Fe^{III} ratio in the NiO/PB cathode was quantified as 1.13 in the original state (Fig. 2f), 1.09 in the oxidized (colored) state, and 1.31 in the reduced (bleached) state. The variation of the Fe^{II}/Fe^{III} ratio indicated that the electrochromic mechanism of NiO/PB lies in the reversible conversion between Fe^{II} and Fe^{III}, Fe^{III} is reduced to Fe^{II} during bleaching and Fe^{II} is oxidized to Fe^{III} during coloration. The configuration of the as-constructed zinc anode-based electrochromic device is shown in Fig. 7a, and its electrochemical reaction can be illustrated in (5)[65]

$$KFe^{III}\,[Fe^{II}\,(CN)_6] + K^+ + e^- \rightleftharpoons K_2Fe^{II}\,[Fe^{II}\,(CN)_6] \quad (5)$$

CV and dynamic transmittance cycling tests were performed to evaluate the cycling performance of the electrochromic devices assembled with different cathodes. The redox peaks around 1.4/1.1 V shown in CV curves of NiO/PB in Fig. 7b correspond to the oxidation and reduction of PB, respectively, which showed excellent electrochemical reversibility and stability after the first cycle activation. In comparison, the CV curves of PB and $Ni(OH)_2$/PB showed an obvious decline in the cycling process (Fig. S13†). This could be attributed to the unique hierarchical structure of NiO/PB that provides fast ion transport kinetics and alleviates the volume expansion during cycling. Fig. 7c demonstrates the dynamic transmittance curves of the zinc anode-based electrochromic device after 1000 cycles. The NiO/PB-based electrochromic device exhibited impressive cycling durability after 1000 cycles, with ΔT retention reaching almost 92%, much higher than both, PB (≈28%) and $Ni(OH)_2$/PB (≈30%). The morphology changes of the cathodes before and after cycling were observed by SEM. NiO/PB cathode showed no significant morphology changes after cycling (Fig. S14†), which is consistent with the excellent electrochromic properties after cycling. However, the bare PB cathode suffered from obvious structural destruction after cycling, leading to serious degradation of the performance. Moreover, long-term cycling tests up to 5000 cycles were employed to further evaluate the cycling durability of NiO/PB-based electrochromic devices. It was shown that 68% of the ΔT was still maintained even after 5000 cycles (Fig. 7d), demonstrating an excellent cycling stability.

To demonstrate the dual-functional electrochromic/energy storage functionalities, a full-cell zinc anode-based electrochromic device (5 × 5 cm^2) was assembled. The initially charged device showed a blue color. Subsequently, the zinc anode-based electrochromic device was employed as a power source to drive the LED display and was then gradually switched from a blue color to a transparent state (Fig. 7e). This clearly indicated that the zinc anode-based electrochromic device served the dual-functions of electrochromic and energy storage. Additionally, a 10 cm × 10 cm zinc anode-based electrochromic device was constructed (Fig. S15†) to demonstrate the potential for large-scale ECES applications.

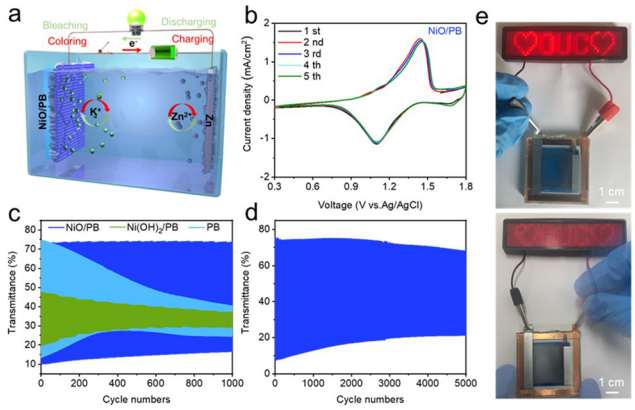

Fig. 7 Characterization of the zinc anode-based electrochromic devices. (a) Schematic description of the working principle of the zinc anode-based electrochromic device. (b) CV curves of the NiO/PB based electrochromic device for the first 5 cycles at 20 mV s^{-1}. (c) Transmittance evolution at potential steps (0.8 V and 1.6 V, each for 20 s) *versus* the number of cycles for PB, $Ni(OH)_2$/PB, and NiO based electrochromic devices. (d) Transmittance evolution curve of NiO/PB based electrochromic device during the long-term cycling. (e) Demonstration of the zinc anode-based electrochromic device as a power source to drive a LED display at charged and discharged states. The device was assembled with NiO/PB//1 M KCl–0.1 M $ZnSO_4$//Zn foil configurations.

Conclusion

In this work, a simple chemical bath deposition method was employed to synthesize uniform and transparent metal oxide interlayer (NiO nanosheets) to improve the electrochemical kinetics and stability of the PB electrode, realizing excellent electrochromic and energy storage performance in NiO/PB. The study showed that the NiO/PB nanocomposite film provided shorter ion diffusion paths and larger specific surface area for the electrolyte uptake, and effectively alleviated the volume expansion in cycling, resulting in fast ion transport kinetics and high charge storage capacity. The NiO/PB electrode offered excellent areal capacity and rate capability, outperforming bare PB and $Ni(OH)_2$/PB. Compared with PB and $Ni(OH)_2$/PB, NiO/PB also enabled superior electrochromic performance in the zinc anode-based electrochromic device with

larger ΔT (73.2%), shorter response time (t_c = 1.4 s, t_b = 2.6 s), and higher CE (54.9 cm^2 C^{-1}) at 632.8 nm. In particular, the NiO/PB-based electrochromic device maintained 92% of the original ΔT after 1000 cycles, which was much higher than that of PB and $Ni(OH)_2$/PB. The transparent metal oxide interlayer greatly facilitated the electrochemical activity, accelerated the electrochemical kinetics, and strengthened the electrochemical stability of PB, rendering simultaneously improved energy storage (areal capacity, rate performance, and cycling stability) and EC performance (ΔT, switching time, CE, and ΔT retention) in the NiO/PB electrode and the zinc anode-based electrochromic device. The excellent energy storage and electrochromic performance of the zinc anode-based electrochromic device will find promising applications in smart multifunctional energy storage and energy-saving devices.

Author contributions

J. W. Chen, H. L. Wang, and H. Z. Li supervised the study. P. Li provided assistance with characterization. Y. Ouyang and Y. Ma contributed to data analysis and manuscript preparation. All authors contributed to the general discussion.

Conflicts of interest

There are no conflicts to declare.

Acknowledgements

This work was supported by the National Natural Science Foundation of China (No. 52202320, 62105185, 22179123), the Fundamental Research Funds for the Central Universities (No. 862201013153, 842312030, 202161076 and 202262010), the Shandong Excellent Young Scientists Fund Program (Overseas) (2023HWYQ-060), Guangdong Basic and Applied Basic Research Foundation (2022A1515011516), and the Taishan Scholar Program of Shandong Province, China (No. tsqn202211048).

References

1 D. Miranda, R. Gonçalves, S. Wuttke, C. M. Costa and S. Lanceros-Méndez, *Adv. Energy Mater.*, 2023, **13**, 2203874.
2 G. Sadeghi, *Energy Storage Mater.*, 2022, **46**, 192–222.
3 Z. Shao, A. Huang, C. Ming, J. Bell, P. Yu, Y.-Y. Sun, L. Jin, L. Ma, H. Luo, P. Jin and X. Cao, *Nat. Electron.*, 2022, **5**, 45–52.
4 J. Yan, S. Huang, Y. V. Lim, T. Xu, D. Kong, X. Li, H. Y. Yang and Y. Wang, *Mater. Today*, 2022, **54**, 110–152.
5 Z. Zhu, T. Jiang, M. Ali, Y. Meng, Y. Jin, Y. Cui and W. Chen, *Chem. Rev.*, 2022, **122**, 16610–16751.
6 C. Wu, H. Shi, L. Zhao, X. Chen, X. Zhang, C. Zhang, J. Yu, Y. Lv, R. Wei, T. Gao, J. Xie, Y. Yu and W. Liu, *Adv. Funct. Mater.*, 2023, **33**, 2214886.
7 K. Wang, H. Wu, Y. Meng, Y. Zhang and Z. Wei, *Energy Environ. Sci.*, 2012, **5**, 8384–8389.
8 S. Zhang, S. Cao, T. Zhang, A. Fisher and J. Y. Lee, *Energy Environ. Sci.*, 2018, **11**, 2884–2892.
9 H. Li, W. Zhang and A. Y. Elezzabi, *Adv. Mater.*, 2020, **32**, 2003574.
10 Y. Ke, J. Chen, G. Lin, S. Wang, Y. Zhou, J. Yin, P. S. Lee and Y. Long, *Adv. Energy Mater.*, 2019, **9**, 1902066.
11 B. Xu, J. Chen, Z. Ding, J. Hu, Y. Zhang, H. Li and H. Wang, *Small Sci.*, 2023, 2300025.
12 S. Cao, S. Zhang, T. Zhang, Q. Yao and J. Y. Lee, *Joule*, 2019, **3**, 1152–1162.
13 J. Chen, A. W. M. Tan, A. L.-S. Eh and P. S. Lee, *Adv. Energy Sustainability Res.*, 2022, **3**, 2100172.
14 C. Gu, A.-B. Jia, Y.-M. Zhang and S. X.-A. Zhang, *Chem. Rev.*, 2022, **122**, 14679–14721.
15 H. Li, L. McRae, C. J. Firby, M. Al-Hussein and A. Y. Elezzabi, *Nano Energy*, 2018, **47**, 130–139.
16 C. G. Granqvist, *Thin Solid Films*, 2014, **564**, 1–38.
17 J. Pan, R. Zheng, Y. Wang, X. Ye, Z. Wan, C. Jia, X. Weng, J. Xie and L. Deng, *Sol. Energy Mater. Sol. Cells*, 2020, **207**, 110337.
18 P. Yang, P. Sun and W. Mai, *Mater. Today*, 2016, **19**, 394–402.
19 Z. Tong, T. Kang, Y. Wan, R. Yang, Y. Wu, D. Shen, S. Liu, Y. Tang and C.-S. Lee, *Adv. Funct. Mater.*, 2021, **31**, 2104639.
20 Y. Ding, M. Wang, Z. Mei and X. Diao, *Sol. Energy Mater. Sol. Cells*, 2022, **248**, 112037.
21 J. Li, P. Yang, X. Li, C. Jiang, J. Yun, W. Yan, K. Liu, H. J. Fan and S. W. Lee, *ACS Energy Lett.*, 2023, **8**, 1–8.
22 H. Li, C. J. Firby and A. Y. Elezzabi, *Joule*, 2019, **3**, 2268–2278.
23 B. Liu, T. Quan, M. Yang, Y. Liu, H. Chen and H. Li, *Chem. Eng. J.*, 2023, **461**, 141925.
24 S.-H. Lee, R. Deshpande, P. A. Parilla, K. M. Jones, B. To, A. H. Mahan and A. C. Dillon, *Adv. Mater.*, 2006, **18**, 763–766.
25 C.-H. Yang, S.-M. Chen, T.-L. Wang and Y.-T. Shieh, *Electrochim. Acta*, 2014, **123**, 268–277.
26 M. Panagopoulou, D. Vernardou, E. Koudoumas, D. Tsoukalas and Y. S. Raptis, *Electrochim. Acta*, 2019, **321**, 134743.
27 Y. Li, Z. Liu, L. Zhao, T. Cui, B. Wang, K. Guo and J. Han, *Electrochim. Acta*, 2015, **173**, 117–123.
28 K. Xu, L. Wang, G. Liu, C. Ge, L. Wang, W. Wang and M. Chen, *Energy Environ. Mater.*, 2023, **6**, e12362.
29 W. Zhang, H. Li and A. Y. Elezzabi, *Adv. Funct. Mater.*, 2023, **33**, 2300155.
30 J. Xu, N. Yuan, J. M. Razal, Y. Zheng, X. Zhou, J. Ding, K. Cho, S. Ge, R. Zhang, Y. Gogotsi and R. H. Baughman, *Energy Storage Mater.*, 2019, **22**, 323–329.
31 P. Ruan, S. Liang, B. Lu, H. J. Fan and J. Zhou, *Angew. Chem., Int. Ed.*, 2022, **61**, e202200598.
32 Y. Li, J. Zhao, Q. Hu, T. Hao, H. Cao, X. Huang, Y. Liu, Y. Zhang, D. Lin, Y. Tang and Y. Cai, *Mater. Today Energy*, 2022, **29**, 101095.

33 M. B. Zakaria and T. Chikyow, *Coord. Chem. Rev.*, 2017, **352**, 328–345.
34 Y. Ding, H. Sun, Z. Li, C. Jia, X. Ding, C. Li, J.-G. Wang and Z. Li, *J. Mater. Chem. A*, 2023, **11**, 2868–2875.
35 M. Kateb, S. Safarian, M. Kolahdouz, M. Fathipour and V. Ahamdi, *Sol. Energy Mater. Sol. Cells*, 2016, **145**, 200–205.
36 Z. Bi, S. Zhang, X. Xu, X. Hu, X. Li and X. Gao, *Mater. Lett.*, 2015, **160**, 186–189.
37 Y. Wang, Z. Gong, Y. Zeng, H. Zhao and J. Yang, *Chem. Eng. J.*, 2022, **431**, 134066.
38 Y. Chen, Z. Bi, X. Li, X. Xu, S. Zhang and X. Hu, *Electrochim. Acta*, 2017, **224**, 534–540.
39 Y.-Y. Song, Z.-D. Gao, J.-H. Wang, X.-H. Xia and R. Lynch, *Adv. Funct. Mater.*, 2011, **21**, 1941–1946.
40 X. Cai, Y. Cai, Y. Liu, S. Deng, Y. Wang, Y. Wang and I. Djerdj, *Ceram. Int.*, 2014, **40**, 57–65.
41 Z. Tang, C.-H. Tang and H. Gong, *Adv. Funct. Mater.*, 2012, **22**, 1272–1278.
42 M. Z. Sialvi, R. J. Mortimer, G. D. Wilcox, A. M. Teridi, T. S. Varley, K. G. U. Wijayantha and C. A. Kirk, *ACS Appl. Mater. Interfaces*, 2013, **5**, 5675–5682.
43 J. Chen, A. L.-S. Eh, J.-H. Ciou and P. S. Lee, *Mater. Today Energy*, 2022, **27**, 101048.
44 G. Li, X. Wang, L. Liu, R. Liu, F. Shen, Z. Cui, W. Chen and T. Zhang, *Small*, 2015, **11**, 731–739.
45 A. Amirzhanova, I. Karakaya, C. B. Uzundal, G. Karaoğlu, F. Karadas, B. Ülgüt and Ö. Dag, *J. Mater. Chem. A*, 2019, **7**, 22012–22020.
46 S. Zhou, S. Wang, S. Zhou, H. Xu, J. Zhao, J. Wang and Y. Li, *Nanoscale*, 2020, **12**, 8934–8941.
47 Z. Bi, X. Li, Y. Chen, X. He, X. Xu and X. Gao, *ACS Appl. Mater. Interfaces*, 2017, **9**, 29872–29880.
48 S. Sarkar, M. Pradhan, A. K. Sinha, M. Basu, Y. Negishi and T. Pal, *Inorg. Chem.*, 2010, **49**, 8813–8827.
49 W. Mao, H. He, P. Sun, Z. Ye and J. Huang, *ACS Appl. Mater. Interfaces*, 2018, **10**, 15088–15095.
50 G. Li, X. Wang, H. Ding and T. Zhang, *RSC Adv.*, 2012, **2**, 13018–13023.
51 M. Mo, J. C. Yu, L. Zhang and S.-K. A. Li, *Adv. Mater.*, 2005, **17**, 756–760.
52 J. Song, L. Wang, Y. Lu, J. Liu, B. Guo, P. Xiao, J.-J. Lee, X.-Q. Yang, G. Henkelman and J. B. Goodenough, *J. Am. Chem. Soc.*, 2015, **137**, 2658–2664.
53 Y. Lu, L. Wang, J. Cheng and J. B. Goodenough, *Chem. Commun.*, 2012, **48**, 6544–6546.
54 Y. You, X.-L. Wu, Y.-X. Yin and Y.-G. Guo, *Energy Environ. Sci.*, 2014, **7**, 1643–1647.
55 H. Gao, S. Xin, L. Xue and J. B. Goodenough, *Chem*, 2018, **4**, 833–844.
56 J. Qian, C. Wu, Y. Cao, Z. Ma, Y. Huang, X. Ai and H. Yang, *Adv. Energy Mater.*, 2018, **8**, 1702619.
57 B. Xie, P. Zuo, L. Wang, J. Wang, H. Huo, M. He, J. Shu, H. Li, S. Lou and G. Yin, *Nano Energy*, 2019, **61**, 201–210.
58 X. W. Sun and J. X. Wang, *Nano Lett.*, 2008, **8**, 1884–1889.
59 X. Gan, X. Li, X. Gao, J. Qiu and F. Zhuge, *Nanotechnology*, 2011, **22**, 305601.
60 G. Moretti and C. Gervais, *J. Raman Spectrosc.*, 2018, **49**, 1198–1204.
61 B. Huang, J. Song, J. Zhong, H. Wang, X. Zheng, J. Jia, S. Yun, D. You, H. Kimura and L. Kang, *Chem. Eng. J.*, 2022, **449**, 137850.
62 M.-S. Wu and H.-H. Hsieh, *Electrochim. Acta*, 2008, **53**, 3427–3435.
63 D. U. Lee, J. Fu, M. G. Park, H. Liu, A. Ghorbani Kashkooli and Z. Chen, *Nano Lett.*, 2016, **16**, 1794–1802.
64 S. Feng, J. Wang, Z. Tong and H.-Y. Qu, *Chem. Eng. J.*, 2022, **442**, 136158.
65 D. Tang, J. Wang, X.-A. Liu, Z. Tong, H. Ji and H.-Y. Qu, *J. Colloid Interface Sci.*, 2023, **636**, 351–362.